

1
2
3
4
5
6
7
8
9
10
11
12
13
14
15
16
17
18
19
20
21
22
23
24
25
26
27
28
29
30
31
32
33

Automated remote focusing, drift correction, and photostimulation to evaluate structural plasticity in dendritic spines

Michael S Smirnov^{1*}, Paul R Evans², Tavita R Garrett¹, Long Yan³, Ryohei Yasuda¹

¹Neuronal Signal Transduction, Max Planck Florida Institute for Neuroscience, Jupiter, Florida, United States of America

²Department of Pharmacology, Emory University School of Medicine, Atlanta, Georgia, United States of America

³Light Microscopy Core, Max Planck Florida Institute for Neuroscience, Jupiter, Florida, United States of America

* Corresponding Author
E-mail: Michael.Smirnov@mpfi.org

34 **Abstract**

35 Long-term structural plasticity of dendritic spines plays a key role in synaptic plasticity, the cellular basis
36 for learning and memory. The biochemical step is mediated by a complex network of signaling proteins
37 in spines. Two-photon imaging techniques combined with two-photon glutamate uncaging allows
38 researchers to induce and quantify structural plasticity in single dendritic spines. However, this method
39 is laborious and slow, making it unsuitable for high throughput screening of factors necessary for
40 structural plasticity. Here we introduce a MATLAB-based module built for Scanimage to automatically
41 track, image, and stimulate multiple dendritic spines. We implemented an electrically tunable lens in
42 combination with a drift correction algorithm to rapidly and continuously track targeted spines and
43 correct sample movements. With a straightforward user interface to design custom multi-position
44 experiments, we were able to adequately image and produce targeted plasticity in multiple dendritic
45 spines using glutamate uncaging. Our methods are inexpensive, open source, and provides up to a
46 five-fold increase in throughput for quantifying structural plasticity of dendritic spines.

47

48 **Introduction**

49 Structural changes in dendritic spines, tiny postsynaptic protrusions on the dendritic surface of neurons,
50 are considered to be the basis of synaptic plasticity, learning, and memory [1-5]. Among several forms
51 of spine structural plasticity, structural long-term potentiation (sLTP) of single dendritic spines has been
52 extensively examined as a structural correlate of functional LTP (fLTP), an electrophysiological model
53 of learning and memory [3, 5, 6]. Applying two-photon glutamate uncaging at a single dendritic spine
54 induces a rapid and long lasting spine enlargement at the stimulated spine, but not the surrounding
55 spines [3]. The signaling cascades necessary for sLTP have been studied by combining sLTP imaging
56 with pharmacological and genetic manipulation. Both sLTP and fLTP depend on NMDA-type glutamate

57 receptors (NDMAR), Ca²⁺/Calmodulin-dependent kinase II (CaMKII) and several small GTPase
58 proteins including Ras, Cdc42, Rac1 and RhoA [4, 7-11]. However, due to the low-throughput nature of
59 the measurement, the study of sLTP has been limited to only a few proteins, and among more than
60 1000 proteins expressed in spines [12-14], it is largely unknown which ones are necessary for spine
61 structural plasticity.

62 The quantification of long-term structural plasticity of dendritic spines requires imaging single spines
63 over extended periods of time (typically ~1 h), and it is necessary to continuously refocus to the target
64 spines. Moreover, in general, imaging and stimulating multiple dendrites over long periods of time has
65 been difficult with regular two-photon microscopy, limiting the throughput of the quantification of spine
66 structural plasticity. Thus, it was necessary to develop a system that allows for 1) automatic focus and
67 drift correction for long-term tracking of dendritic spines and 2) imaging and stimulation of several
68 regions of interests (ROIs).

69 Although automated focusing for microscopy is a well-studied topic in literature [15-22], most algorithms
70 are designed for highly specific imaging modes and preparations. These techniques have been tested
71 under well-defined parameters, therefore, their application in a novel paradigm often results in an
72 overwhelming amount of trial-and-error. Algorithms tend to be uniquely suited to either bright-field,
73 phase, or fluorescence microscopy [23]. A lack of functional specificity for software focusing has led
74 some groups to development more inclusive algorithms [20], but the wide variety of imaging setups and
75 biological preparations leaves these attempts incomplete. Hardware focusing systems that correct
76 focus by tracking coverslip location are also commercially available [24], but are incapable of correcting
77 focus drift due to sample deformation which occurs in soft neuronal tissue such as brain slices. In order
78 to optimize software focusing for dendritic spine imaging, an automated algorithm selection tool is
79 necessary to best adapt to the optical parameters and tissue characteristics in the experiment. In
80 addition, since live neuronal tissue can be highly sensitive to objective movements, it is necessary to
81 use a focusing system without objective movements, e.g. an electro-tunable lens (ETL) [25-27].

82 Based on the open-source MATLAB imaging suite Scanimage [28] and an ETL, we have developed an
83 automated system to stimulate and image several individual spines over extended periods of time. With
84 the implementation of an ETL and custom tracking software, our system avoids any artifacts caused by
85 objective or stage movement. We demonstrate that this system allows us to rapidly quantify sLTP in
86 large number of spines.

87

88 Results

89 In order to achieve rapid and reliable focusing required for auto-focusing system, we employed ETL to
90 our two-photon microscope by placing it at a conjugate plane of the back-focal plane of the objective
91 (Fig 1A). A pre-ETL lens resizes the beam to fit the full aperture of the ETL, while two more lenses
92 serve to resize the beam to fit the galvanometers. In this setup, regardless of ETL shape, the beam size
93 is constant at the galvanometers and the back aperture plane of the objective. This setup minimizes the
94 loss of beam intensity and spherical aberration.

95 **Fig 1. ETL installed in the excitation path and controlled via software GUIs.** (A) An ETL in the excitation pathway shapes
96 the incoming beam for remote focusing. Beam shape (red/green) is controlled by curvature of the ETL. L2 and L3 lenses are
97 placed to conjugate the ETL to the back aperture of the objective lens. (B) A GUI controls ETL shape. Voltage values are
98 translated to Z position, and the relative shift of the imaging plane is previewed in a 3D graphic. Z values corresponding to
99 voltages are set either by a linear constant or polynomial curve. (C) ETL voltages are correlated to linear stage movements
100 using an automated alignment routine. (D) Tilted imaging is previewed by adjusting voltage range, as the ETL voltage is
101 altered in phase with the slow-scanning galvanometer.

102 We controlled the focal length of ETL by changing current passing through the lens using a custom
103 interface built into Scanimage using Matlab (Fig 1B). Initial tuning of the ETL is accomplished by
104 stepwise movement of a Z motor combined with an autofocusing step using solely the ETL. The
105 resulting voltages used to control the ETL are automatically associated with Z displacement values,
106 while a conversion function is set using either a linear constant or polynomial fitted curve (Fig 1 B,C). A

107 3D preview of the imaging plane shows the relative position of the Z plane as a result of ETL offset.
108 Finally, by varying the ETL current in phase with the galvanometer scanning cycle, we were able to tilt
109 the imaging plane, thus allowing users to capture objects which would otherwise require multiple Z
110 slices [27] (Fig 1D).

111 In order to make long-term imaging possible, we added an interface to compensate for both axial and
112 lateral drift (Fig 2B). Before the start of imaging, users define the range, step size, and frequency
113 parameters for an autofocus routine. When Z-stacks are collected, images are automatically used for
114 auto-focusing. A region of interest (ROI) is defined around the dendritic spine to be stimulated. In order
115 to expand the applicability of our autofocus module to various imaging setups, we have included 30
116 different autofocusing algorithms, previously described by Pertuz et al. [29]. To test the appropriate
117 algorithm for our purpose, we designed an additional application which tests each algorithm against a
118 set of pre-acquired Z stack images, comparing both accuracy and computation time (Fig 2A). In order
119 to ensure that the autofocus algorithm is running normally and using the appropriate part of an image,
120 each collected slice is displayed along with its respective ROI and Z position (Fig 2D). Finally, lateral
121 drift is measured by comparing the imaged position with a reference image by calculating cross-
122 correlation (8), and corrected by immediately shifting the galvanometer scanning angle. While both
123 autofocus and lateral drift correction speeds are dependent on the pixel count of an image, the speed of
124 calculation for a 128x128 pixel image is consistently less than 10 ms (Fig 2D), far exceeding the speed
125 required for most imaging setups.

126 **Fig 2. Custom autofocus and drift correction parameters track spines over time.** (A) Sample result of the autofocus
127 algorithm selection tool based on 30 Z stacks with 6 slices each. All algorithms adapted from Pertuz, et al. [29]. Abbreviations
128 expanded in Table 1. Percent relative accuracy (gray bars) indicates standardized mean distance of Z position selected by
129 algorithm vs target. 100% = no distance, 0% = maximum distance, 50% = distance if position is picked at random. Blue lines
130 indicate average time to calculate focus value for each slice. (B) Focus and drift correction is controlled through a GUI. Users
131 identify an algorithm, Z range and amount of steps, and whether extra images are collected for autofocus. Drift correction can
132 be enabled to use galvanometers (scan shift) or motor repositioning. Users also have the option to enable or disable the ETL.

133 (D) Reference-based drift correction speed is correlated with pixel size. Image resolution indicates pixel count for one
134 dimension of a square image. (C) Live updates inform users of the selected focus position (green box) and spine ROI used to
135 determine relative focus value (red box).

136 **Table 1. Abbreviations for autofocus operators**

ACMO	Absolute central moment [30]
BREN	Brenner's focus measure [21]
CONT	Image contrast [31]
CURV	Image curvature [32]
DCTE	DCT Energy measure [18]
DCTR	DCT Energy ratio [33]
GDER	Gaussian derivative [20]
GLVA	Gray-level variance [34]
GLLV	Gray-level local variance [35]
GLVN	Gray-level variance normalized [21]
GRAE	Energy of gradient [36]
GRAT	Thresholded gradient [21]
GRAS	Squared gradient [37]
HELM	Helmi's measure [32]
HISE	Histogram entropy [34]
HISR	Histogram range [22]
LAPE	Energy of Laplacian [36]
LAPM	Modified Laplacian [38]
LAPV	Variance of Laplacian [35]
LAPD	Diagonal Laplacian [39]
SFIL	Steerable filters-based [40]
SFRQ	Spatial frequency [37]
TENG	Tenegrad [34]
TENV	Tenegrad variance [35]
VOLA	Vollat's correlation-based [21]
BRGT	Maximum Brightness
MGRD	Maximum Brightness Gradient

137

138 In addition, we designed a user-friendly interface to rapidly find, store, image, and stimulate multiple
139 positions (Fig 3). Either motor or scanning controls are used to identify dendritic spines for
140 photostimulation (glutamate uncaging). As positions are defined, reference images are automatically
141 collected (Fig 3D). Once all positions are defined, all motor positions are mapped to galvanometer

142 scanning angles (Fig 3A). A separate window allows users to design a timeline for their experiment (Fig
143 3B). The timeline allows users to control imaging frequency, duration, and define when glutamate
144 uncaging will occur to stimulate dendritic spines. Timeline events can be staggered between positions
145 to avoid conflict between successive uncaging or exclusive imaging events. If the amount of defined
146 positions exceeds the maximum which could be concurrently imaged within a given time constraint, new
147 positions are rotated into the imaging sessions as imaging for other positions is completed (Fig 3B). As
148 imaging proceeds, each position is continuously updated using its reference image (Fig 3D), while an
149 automatic re-alignment of the photoactivation ROI to the cell membrane immediately precedes
150 photoactivation (Fig 3E).

151 **Fig 3. Non-motorized, automated, multi-position ROI selection, imaging, and photoactivation is controlled through a**
152 **user-friendly interface.** (A) GUI showing all motor positions that are translated to galvanometer scanning coordinates within a
153 single field of view (FOV, large square). (B) A custom timeline interface allows users to design and preview imaging and (blue,
154 green) and uncaging (red) cycles at each position. (C) A master GUI to keep track of and move between all imaging positions.
155 Settings and coordinates can be saved and loaded. Z depth is set for each position to automatically modulate uncaging laser
156 power to amounts of tissue interference in brain slices. Experimental Notes are automatically saved with each imaging cycle
157 and can be altered to reflect experimental parameters. (D) GUI showing reference images for each position. Reference images
158 are used for drift correction. Zoomed out reference images (right) are used for initial alignment. Threshold intensity values are
159 set so each uncaging ROI (E, red) is shifted appropriately relative to the cell dendrite perimeter (E, blue).

160 To test and further optimize the efficacy of our non-motor multi-position imaging system, we measured
161 structural plasticity of dendritic spines in hippocampal CA1 neurons transfected with enhanced green
162 fluorescent protein (EGFP) in organotypic hippocampal slice prepared from mice (Fig 4). The lateral
163 and axial drift corrections successfully tracked most spines and dendrites for a long time regardless of
164 morphological changes. However, the spine set to be stimulated sometimes moves relative to the
165 dendrite. Since glutamate uncaging had to be precisely targeted to the surface of the spine, we added a
166 secondary drift correction method which would relocate the uncaging target to the surface of the spine
167 immediately prior to uncaging. This allowed automated glutamate uncaging on multiple spines at
168 consistent locations at the spine surface. We found that glutamate uncaging induced a rapid increase in

169 volume within few minutes (transient phase) followed by long lasting enlargement (sustained phase),
170 consistent with previous studies [3, 10, 41]. During the whole imaging session, the user did not need to
171 be at the microscope, demonstrating the capability of automated tracking and stimulating software.

172 **Fig 4. Plasticity in dendritic spines induced using automated focus, drift correction, and glutamate uncaging.** (Top)
173 CA1 dendrite pre- and post- uncaging. Arrow indicates photoactivation ROI. Scale = 1 μ m. Middle: Average volume change in
174 spines following glutamate uncaging at t=0. Uncaging lasts 60s. Bottom: Quantification of transient (1-3 min) and sustained
175 (26-30 min) change in spine volume. **** = p<0.0001, * = p<0.05. n=24 Stimulated spines, 7 neurons.

176

177 **Discussion**

178 We have designed an easily implementable module for Scanimage to allow for multi-position scanning
179 and photoactivation of dendritic spines to study postsynaptic plasticity. Furthermore, we described an
180 implementation of an ETL in the excitation path which minimizes the signal loss and distortion. The ETL
181 served both to increase imaging speed and remove sample drift caused by rapid stage or objective
182 movements when changing focus. Our optical implementation of the ETL as a remote focusing element
183 is combined with a straightforward user interface which is able to align and control the ETL current, and
184 as a result, the axial focus. Furthermore, our software interface allows users to tilt the imaging plane in
185 3D by rapidly modulating the axial focus position in phase with the Y-scanning galvanometer. We
186 expect this feature to be particularly useful in neuroscience, where long, straight neuronal projections
187 can be scanned along their own axis, resulting in a significant increase in scanning efficiency. We found
188 that an ETL-based system is relatively low price and easily implemented in any two-photon microscope.
189 While the focusing speed of an ETL (15 ms) is sufficient for multi-position imaging, tilted-plane imaging
190 needs to be performed fairly slowly, at around 1Hz, to allow the ETL sufficient refocusing time along the
191 imaging plane.

192 It should be noted that there are faster (but more expensive and potentially more complicated) focusing
193 devices which could be used with our software. For example, spatial light modulators (SLMs) can
194 create 3D holograms within 2-4 ms, and have adaptive optics capabilities to potentially decrease
195 distortion and aberration [42-44]. A focusing device using a secondary objective and a galvanic mirror
196 [45] provides even faster focus movement (~ 1 ms). Perhaps the most well-established remote focusing
197 element is the acoustic optic deflector (AOD), which can provide high-performance volume imaging in
198 tissue [46, 47].

199 As for controlling software, we implemented a highly capable and customizable focus and drift
200 correction system in order to broaden biological applications. Previously, dozens of autofocus
201 algorithms have been made available through primary literature and open source code [20]. However,
202 these algorithms were not extensively implemented. Since imaging conditions may be drastically
203 different for many users, we designed a tool capable of narrowing down the optimal algorithm based on
204 accuracy and speed (Fig 3B). This allowed us to optimize our autofocusing algorithm to spine imaging
205 experiments.

206 Finally, in order to allow the software to optimize experiments for biological events occurring at multiple
207 time scales, we introduced a modular timeline scheduling feature which allows users to designate
208 custom timeframes for imaging and photo-stimulation. This feature was especially important for
209 studying sLTP, which has two distinct phases at different time scales (Fig. 4). During transient phase
210 (first ~5 min following stimulation), it is crucial to acquire images with higher frequency (typically ~10 –
211 60 s per image) since the volume change is rapid. However, during the steady state (~10 – 60 min),
212 spine volume is stable and fast acquisition is unnecessary and rather damaging to the sample. The
213 typical sampling time for the steady state is ~2 – 20 min. We demonstrated that this implementation
214 allows us to measure the time course of sLTP in several spines (so far up to ~5 spines) with high
215 efficiency.

216

217 **Conclusion**

218 We successfully designed and implemented an automated system capable of reliably measuring sLTP
219 in multiple dendritic spines. The implementation of an ETL in the excitation path, combined with
220 galvanic mirror scanning, allowed us to quickly switch between imaging positions with minimum
221 perturbation to the sample. The customizable autofocus and drift correction system allows our software
222 to track and stimulate individual dendritic spines over extended imaging sessions. By dramatically
223 increasing the throughput of spine imaging and stimulation experiments, our system will accelerate
224 studies to understand molecular basis of spine structural plasticity. In addition, the flexible
225 implementation of software would allow researchers to use it for many imaging/photostimulation
226 experiments.

227

228 **Methods**

229 **ETL Implementation:** An EL-10-30 ETL (Optotune) was implemented in the excitation
230 pathway (Fig 1). The light path was designed in OpticStudio (Zemax) and optimized during setup so the
231 ETL is conjugated to the back aperture of the objective. Lens L1 shapes the beam to fill the ETL. L2
232 and L3 are used to conjugate the ETL to the back aperture of the objective. A typical scan lens and
233 tube lens setup passes the beam to the objective. The ETL is controlled by a current range of 0-300mA
234 as indicated in the manual.

235 **Software Design:** All programming was done in MATLAB to be compatible with Scanimage
236 3.8, available online for free (<http://scanimage.vidriotechnologies.com>). Autofocus and drift correction
237 functions were implemented based on published code [29, 48]. Abbreviations for focus measure
238 operators are listed in Table 1. Maximum Brightness (BRGT) assigns focus values based on the

239 maximum pixel intensity within the image. Maximum Brightness Gradient (MGRD) assigns focus values
240 based on the maximum gradient magnitude value of the image. Drift correction in XY is calculated
241 using a built-in MATLAB 2D cross-correlation algorithm [48].

242 **Evaluation of plasticity:** Mouse pups were euthanized by deep anesthesia by isoflurane
243 followed by decapitation. Organotypic hippocampal slice cultures were prepared as described
244 previously [49] from p4-p6 mice and were cultured for 10-12 days before transfection. A biolistic
245 particle delivery system (Helios® Gene Gun System, Bio-Rad) was used to introduce fluorescent GFP
246 labels to obtain sparse transfection of neurons. Two to six days after transfection, neurons in sparsely
247 GFP-labeled CA1 hippocampal regions were chosen for imaging. Individual spines in the striatum
248 radiatum on secondary apical dendrites were chosen for observation. MNI-caged L-glutamate (4-
249 methoxy-7-nitroindolinyI-caged L-glutamate, Tocris) was uncaged with a train of 820-nm laser pulses
250 (3.5–4 mW under the objective, 30 times at 1 Hz) near a spine of interest. Pulse duration was varied 4-
251 8ms based on depth of the spine in tissue, allowing for reliable uncaging without excess light exposure.
252 Experiments were performed at room temperature in ACSF solution containing (in mM): 127 NaCl, 2.5
253 KCl, 25 NaHCO₃, 1.25 NaH₂PO₄, 4 CaCl₂, 25 glucose, 0.001 tetrodotoxin (Tocris) and 4 MNI-caged
254 L-glutamate, bubbled with 95% O₂ and 5% CO₂. All animal procedures were approved by the Max
255 Planck Florida Institute for Neuroscience Animal Care and Use Committee, in accordance with
256 guidelines by the US National Institutes of Health.

257 **Quantification and statistics:** Spine volume was quantified using custom software
258 written in MATLAB; all Z slices were summed together and oval and polygonal ROIs were drawn to
259 select spines and dendrites, respectively. Volumes for each object were standardized to their average
260 pre-uncaging values. Statistical significance was obtained using unpaired t-tests comparing the
261 stimulated spine and adjacent spine averages to the dendrite as a control.

262 **References:**

- 263 1. Bailey CH, Kandel ER, Harris KM. Structural Components of Synaptic Plasticity and Memory
264 Consolidation. *Cold Spring Harb Perspect Biol.* 2015;7(7):a021758. doi: 10.1101/cshperspect.a021758.
265 PubMed PMID: 26134321.
- 266 2. Fu M, Yu X, Lu J, Zuo Y. Repetitive motor learning induces coordinated formation of clustered
267 dendritic spines in vivo. *Nature.* 2012;483(7387):92-5. doi: 10.1038/nature10844. PubMed PMID:
268 22343892; PubMed Central PMCID: PMCPMC3292711.
- 269 3. Matsuzaki M, Honkura N, Ellis-Davies GC, Kasai H. Structural basis of long-term potentiation in
270 single dendritic spines. *Nature.* 2004;429(6993):761-6. doi: 10.1038/nature02617. PubMed PMID:
271 15190253; PubMed Central PMCID: PMCPMC4158816.
- 272 4. Kim IH, Wang H, Soderling SH, Yasuda R. Loss of Cdc42 leads to defects in synaptic plasticity
273 and remote memory recall. *Elife.* 2014;3:e02839-e. doi: 10.7554/eLife.02839. PubMed PMID:
274 25006034; PubMed Central PMCID: PMCPMC4115656.
- 275 5. Hayashi-Takagi A, Yagishita S, Nakamura M, Shirai F, Wu YI, Loshbaugh AL, et al. Labelling
276 and optical erasure of synaptic memory traces in the motor cortex. *Nature.* 2015;525(7569):333-8. doi:
277 10.1038/nature15257. PubMed PMID: 26352471; PubMed Central PMCID: PMCPMC4634641.
- 278 6. Wilbrecht L, Holtmaat A, Wright N, Fox K, Svoboda K. Structural plasticity underlies experience-
279 dependent functional plasticity of cortical circuits. *J Neurosci.* 2010;30(14):4927-32. doi:
280 10.1523/JNEUROSCI.6403-09.2010. PubMed PMID: 20371813; PubMed Central PMCID:
281 PMCPMC2910869.
- 282 7. Colgan LA, Yasuda R. Plasticity of dendritic spines: subcompartmentalization of signaling. *Annu*
283 *Rev Physiol.* 2014;76:365-85. doi: 10.1146/annurev-physiol-021113-170400. PubMed PMID:
284 24215443; PubMed Central PMCID: PMCPMC4142713.

- 285 8. Lee SJ, Escobedo-Lozoya Y, Szatmari EM, Yasuda R. Activation of CaMKII in single dendritic
286 spines during long-term potentiation. *Nature*. 2009;458(7236):299-304. doi: 10.1038/nature07842.
287 PubMed PMID: 19295602; PubMed Central PMCID: PMCPMC2719773.
- 288 9. Lisman J, Yasuda R, Raghavachari S. Mechanisms of CaMKII action in long-term potentiation.
289 *Nat Rev Neurosci*. 2012;13(3):169-82. doi: 10.1038/nrn3192. PubMed PMID: 22334212; PubMed
290 Central PMCID: PMCPMC4050655.
- 291 10. Murakoshi H, Wang H, Yasuda R. Local, persistent activation of Rho GTPases during plasticity
292 of single dendritic spines. *Nature*. 2011;472(7341):100-4. doi: 10.1038/nature09823. PubMed PMID:
293 21423166; PubMed Central PMCID: PMCPMC3105377.
- 294 11. Rex CS, Chen LY, Sharma A, Liu J, Babayan AH, Gall CM, et al. Different Rho GTPase-
295 dependent signaling pathways initiate sequential steps in the consolidation of long-term potentiation. *J*
296 *Cell Biol*. 2009;186(1):85-97. doi: 10.1083/jcb.200901084. PubMed PMID: 19596849; PubMed Central
297 PMCID: PMCPMC2712993.
- 298 12. Bayes A, van de Lagemaat LN, Collins MO, Croning MD, Whittle IR, Choudhary JS, et al.
299 Characterization of the proteome, diseases and evolution of the human postsynaptic density. *Nat*
300 *Neurosci*. 2011;14(1):19-21. doi: 10.1038/nn.2719. PubMed PMID: 21170055; PubMed Central PMCID:
301 PMCPMC3040565.
- 302 13. Fernandez E, Collins MO, Uren RT, Kopanitsa MV, Komiyama NH, Croning MD, et al. Targeted
303 tandem affinity purification of PSD-95 recovers core postsynaptic complexes and schizophrenia
304 susceptibility proteins. *Mol Syst Biol*. 2009;5(269):269. doi: 10.1038/msb.2009.27. PubMed PMID:
305 19455133; PubMed Central PMCID: PMCPMC2694677.
- 306 14. Collins MO, Husi H, Yu L, Brandon JM, Anderson CN, Blackstock WP, et al. Molecular
307 characterization and comparison of the components and multiprotein complexes in the postsynaptic

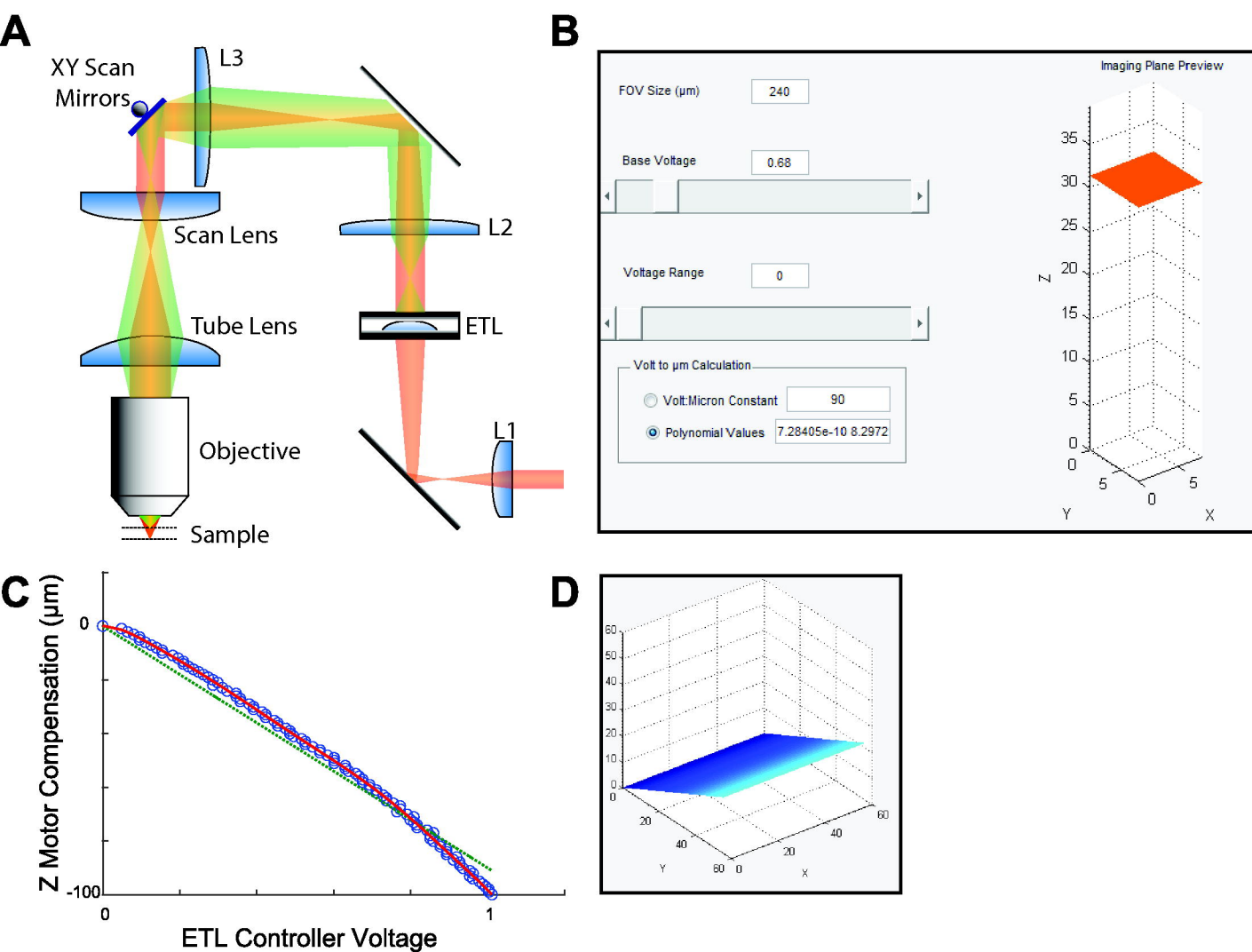
- 308 proteome. J Neurochem. 2006;97 Suppl 1(m):16-23. doi: 10.1111/j.1471-4159.2005.03507.x. PubMed
309 PMID: 16635246.
- 310 15. Redondo R, Bueno G, Valdiviezo JC, Nava R, Cristobal G, Deniz O, et al. Autofocus evaluation
311 for brightfield microscopy pathology. J Biomed Opt. 2012;17(3):036008. doi:
312 10.1117/1.JBO.17.3.036008. PubMed PMID: 22502566.
- 313 16. Zhang ZC, Xia SR. [An autofocus algorithm based on principal component analysis]. Zhongguo
314 Yi Liao Qi Xie Za Zhi. 2008;32(6):391-3, 7. PubMed PMID: 19253566.
- 315 17. Bravo-Zanoguera ME, Laris CA, Nguyen LK, Oliva M, Price JH. Dynamic autofocus for
316 continuous-scanning time-delay-and-integration image acquisition in automated microscopy. J Biomed
317 Opt. 2007;12(3):034011. doi: 10.1117/1.2743078. PubMed PMID: 17614719.
- 318 18. Shen F, Hodgson L, Hahn K. Digital autofocus methods for automated microscopy. Methods
319 Enzymol. 2006;414:620-32. doi: 10.1016/S0076-6879(06)14032-X. PubMed PMID: 17110214.
- 320 19. Marks DL, Oldenburg AL, Reynolds JJ, Boppart SA. Autofocus algorithm for dispersion
321 correction in optical coherence tomography. Appl Opt. 2003;42(16):3038-46. PubMed PMID: 12790455.
- 322 20. Geusebroek JM, Cornelissen F, Smeulders AW, Geerts H. Robust autofocusing in microscopy.
323 Cytometry. 2000;39(1):1-9. PubMed PMID: 10655557.
- 324 21. Santos A, Ortiz de Solorzano C, Vaquero JJ, Pena JM, Malpica N, del Pozo F. Evaluation of
325 autofocus functions in molecular cytogenetic analysis. J Microsc. 1997;188(Pt 3):264-72. PubMed
326 PMID: 9450330.
- 327 22. Firestone L, Cook K, Culp K, Talsania N, Preston K, Jr. Comparison of autofocus methods for
328 automated microscopy. Cytometry. 1991;12(3):195-206. Epub 01/01. doi: 10.1002/cyto.990120302.
329 PubMed PMID: 2036914.

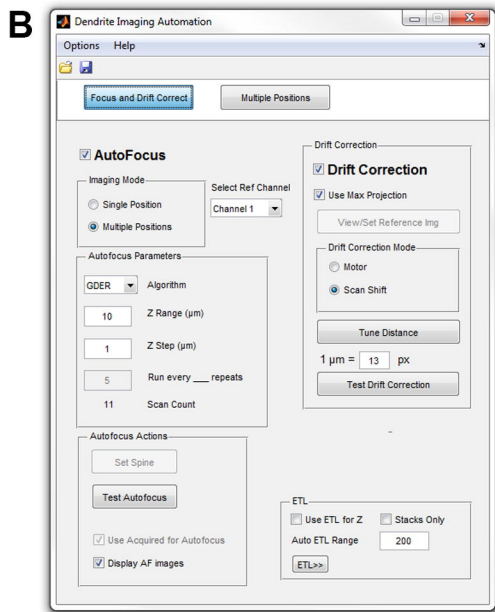
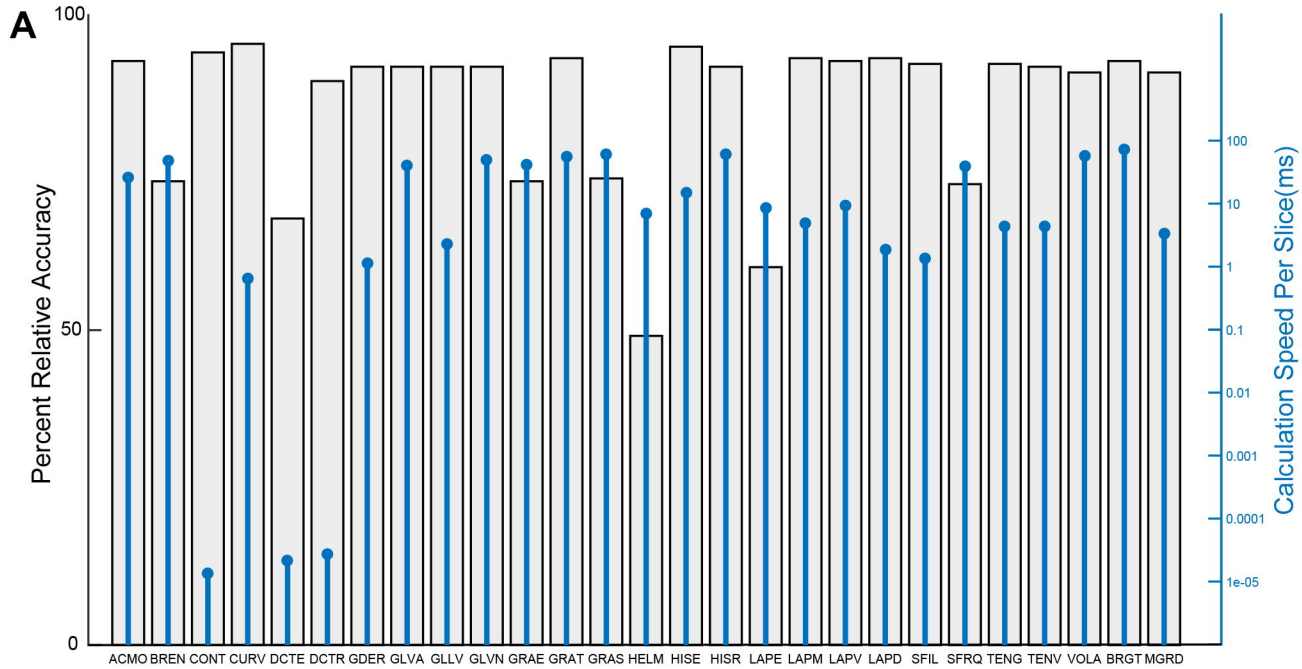
- 330 23. Price JH, Gough DA. Comparison of phase-contrast and fluorescence digital autofocus for
331 scanning microscopy. *Cytometry*. 1994;16(4):283-97. doi: 10.1002/cyto.990160402. PubMed PMID:
332 7988291.
- 333 24. Fairley CR, Thompson TV, Lee KK. Method and apparatus for automatic focusing of a confocal
334 laser microscope. Google Patents; 1997.
- 335 25. Jabbour JM, Malik BH, Olsovsky C, Cuenca R, Cheng S, Jo JA, et al. Optical axial scanning in
336 confocal microscopy using an electrically tunable lens. *Biomed Opt Express*. 2014;5(2):645-52. doi:
337 10.1364/BOE.5.000645. PubMed PMID: 24575357; PubMed Central PMCID: PMC3920893.
- 338 26. Chen JL, Pfaffli OA, Voigt FF, Margolis DJ, Helmchen F. Online correction of licking-induced
339 brain motion during two-photon imaging with a tunable lens. *J Physiol*. 2013;591(19):4689-98. doi:
340 10.1113/jphysiol.2013.259804. PubMed PMID: 23940380; PubMed Central PMCID:
341 PMC3800448.
- 342 27. Grewe BF, Voigt FF, van 't Hoff M, Helmchen F. Fast two-layer two-photon imaging of neuronal
343 cell populations using an electrically tunable lens. *Biomed Opt Express*. 2011;2(7):2035-46. doi:
344 10.1364/BOE.2.002035. PubMed PMID: 21750778; PubMed Central PMCID: PMC3130587.
- 345 28. Pologruto TA, Sabatini BL, Svoboda K. ScanImage: flexible software for operating laser
346 scanning microscopes. *Biomed Eng Online*. 2003;2(1):13. doi: 10.1186/1475-925X-2-13. PubMed
347 PMID: 12801419; PubMed Central PMCID: PMC3130587.
- 348 29. Pertuz S, Puig D, Garcia MA. Analysis of focus measure operators for shape-from-focus.
349 *Pattern Recognition*. 2013;46(5):1415-32. doi: 10.1016/j.patcog.2012.11.011.
- 350 30. Shirvaikar M, editor An optimal measure for camera focus and exposure. Proceedings of the
351 Thirty-Sixth Southeastern Symposium on System Theory (SSST04); 2004.

- 352 31. Harsh Nanda RC, editor Practical calibrations for a real-time digital omnidirectional camera. In
353 Technical Sketches, Computer Vision and Pattern Recognition; 2001.
- 354 32. Helmlí FS, Scherer S, editors. Adaptive shape from focus with an error estimation in light
355 microscopy. Image and Signal Processing and Analysis, 2001 ISPA 2001 Proceedings of the 2nd
356 International Symposium on; 2001: IEEE.
- 357 33. Lee S-Y, Yoo J-T, Kumar Y, Kim S-W. Reduced Energy-Ratio Measure for Robust Autofocusing
358 in Digital Camera. IEEE Signal Processing Letters. 2009;16(2):133-6. doi: 10.1109/lsp.2008.2008938.
- 359 34. Krotkov E, Martin J-P, editors. Range from focus. Robotics and Automation Proceedings 1986
360 IEEE International Conference on; 1986: IEEE.
- 361 35. Pech-Pacheco JL, Cristóbal G, Chamorro-Martinez J, Fernández-Valdivia J, editors. Diatom
362 autofocusing in brightfield microscopy: a comparative study. Pattern Recognition, 2000 Proceedings
363 15th International Conference on; 2000: IEEE.
- 364 36. Nikzad MSTSCA. Focusing Techniques. Journal of Optical Engineering. 1993:2824-36.
- 365 37. Eskicioglu AM, Fisher PS. Image quality measures and their performance. IEEE Transactions
366 on communications. 1995;43(12):2959-65.
- 367 38. Nayar SK, Nakagawa Y, editors. Shape from focus: an effective approach for rough surfaces.
368 Robotics and Automation, 1990 Proceedings, 1990 IEEE International Conference on; 1990: IEEE.
- 369 39. Thelen A, Frey S, Hirsch S, Hering P. Improvements in shape-from-focus for holographic
370 reconstructions with regard to focus operators, neighborhood-size, and height value interpolation. IEEE
371 Trans Image Process. 2009;18(1):151-7. Epub 12/20. doi: 10.1109/TIP.2008.2007049. PubMed PMID:
372 19095526.

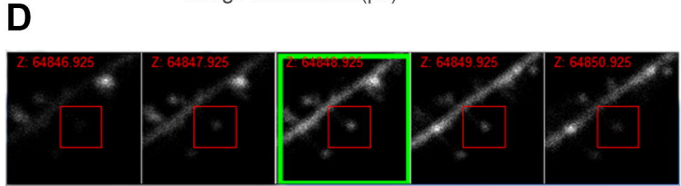
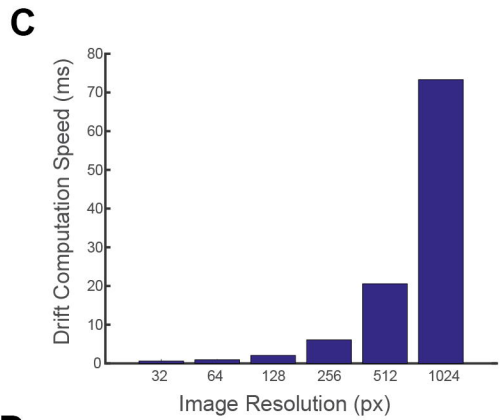
- 373 40. Windsor RM, Univeresity of W, Abdul AM, Univeresity of W, Wu QMJ, Univeresity of W, et al.,
374 editors. 3D Shape from Focus and Depth Map Computation Using Steerable Filters. ICIAR; 2016:
375 Springer Berlin Heidelberg.
- 376 41. Murakoshi H, Lee SJ, Yasuda R. Highly sensitive and quantitative FRET-FLIM imaging in single
377 dendritic spines using improved non-radiative YFP. *Brain Cell Biol.* 2008;36(1-4):31-42. doi:
378 10.1007/s11068-008-9024-9. PubMed PMID: 18512154; PubMed Central PMCID: PMCPMC2673728.
- 379 42. Yang W, Miller JE, Carrillo-Reid L, Pnevmatikakis E, Paninski L, Yuste R, et al. Simultaneous
380 Multi-plane Imaging of Neural Circuits. *Neuron.* 2016;89(2):269-84. doi: 10.1016/j.neuron.2015.12.012.
381 PubMed PMID: 26774159; PubMed Central PMCID: PMCPMC4724224.
- 382 43. Lutz C, Otis TS, DeSars V, Charpak S, DiGregorio DA, Emiliani V. Holographic photolysis of
383 caged neurotransmitters. *Nat Methods.* 2008;5(9):821-7. doi: 10.1038/nmeth.1241. PubMed PMID:
384 19160517; PubMed Central PMCID: PMCPMC2711023.
- 385 44. Nikolenko V, Watson BO, Araya R, Woodruff A, Peterka DS, Yuste R. SLM Microscopy:
386 Scanless Two-Photon Imaging and Photostimulation with Spatial Light Modulators. *Front Neural*
387 *Circuits.* 2008;2(December):5. doi: 10.3389/neuro.04.005.2008. PubMed PMID: 19129923; PubMed
388 Central PMCID: PMCPMC2614319.
- 389 45. Botcherby EJ, Smith CW, Kohl MM, Debarre D, Booth MJ, Juskaitis R, et al. Aberration-free
390 three-dimensional multiphoton imaging of neuronal activity at kHz rates. *Proc Natl Acad Sci U S A.*
391 2012;109(8):2919-24. doi: 10.1073/pnas.1111662109. PubMed PMID: 22315405; PubMed Central
392 PMCID: PMCPMC3286923.
- 393 46. Duemani Reddy G, Kelleher K, Fink R, Saggau P. Three-dimensional random access
394 multiphoton microscopy for functional imaging of neuronal activity. *Nat Neurosci.* 2008;11(6):713-20.
395 doi: 10.1038/nn.2116. PubMed PMID: 18432198; PubMed Central PMCID: PMCPMC2747788.

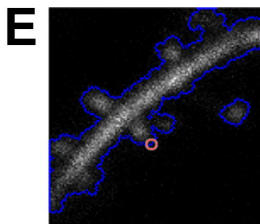
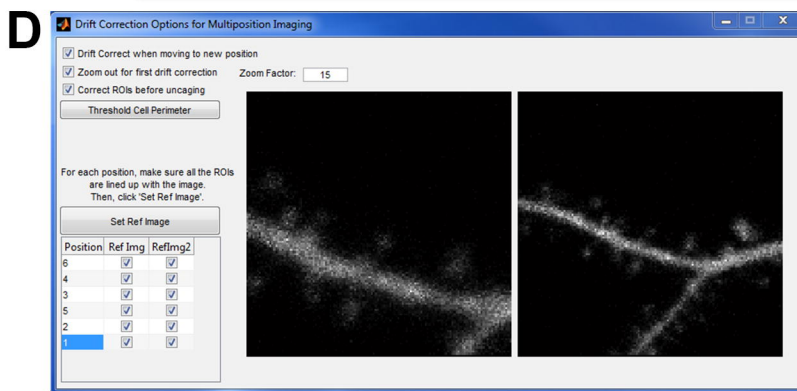
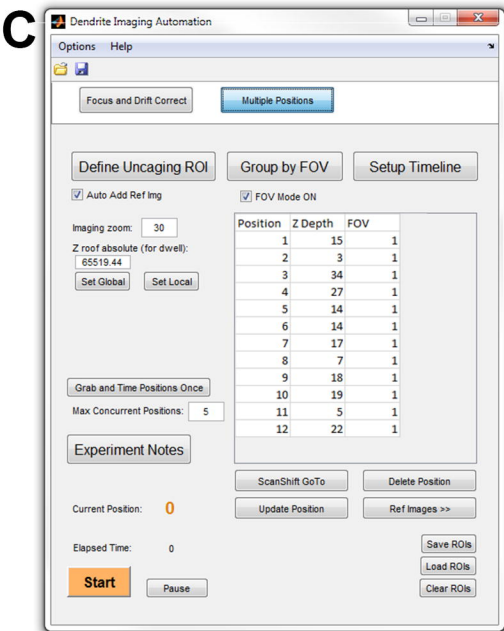
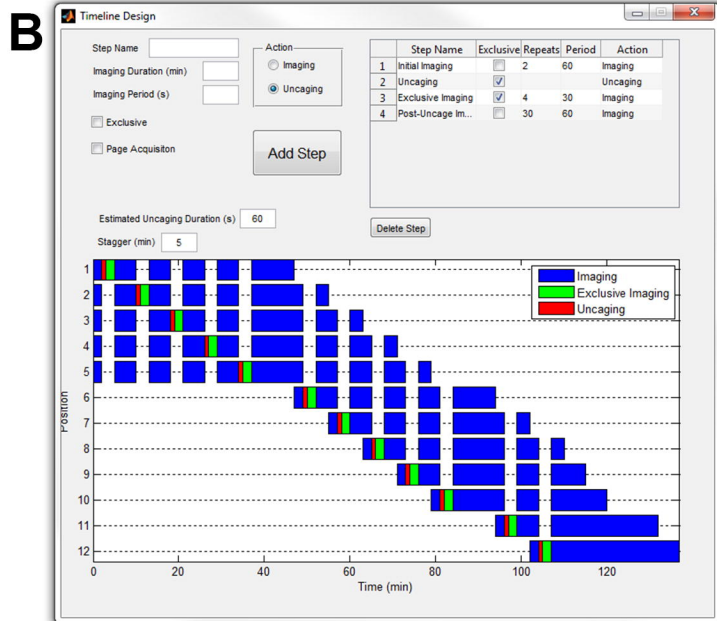
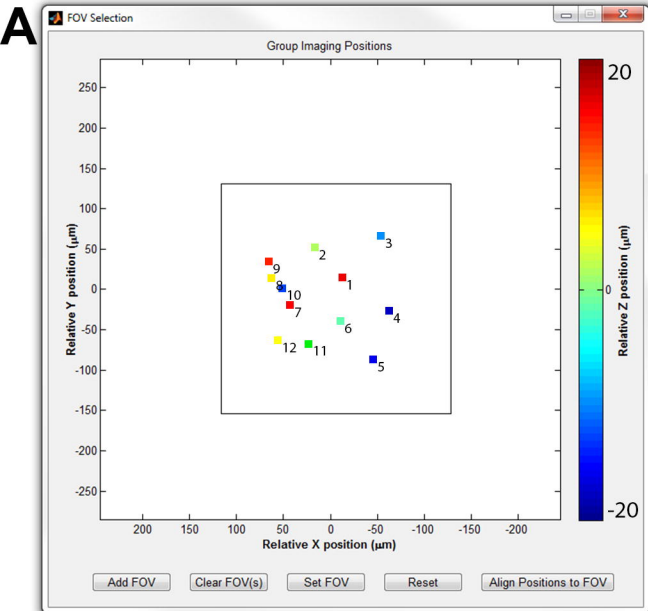
- 396 47. Kirkby PA, Srinivas NKMN, Silver RA. Europe PMC Funders Group Europe PMC Funders
397 Author Manuscripts A compact acousto-optic lens for 2D and 3D femtosecond based 2-photon
398 microscopy. 2010;18(13):13721-45.
- 399 48. Sugar JD, Cummings AW, Jacobs BW, Robinson DB. A Free Matlab Script for Spatial Drift
400 Correction. Microscopy Today. 2014;22(05):40-7. doi: 10.1017/s1551929514000790.
- 401 49. Stoppini L, Buchs PA, Muller D. A simple method for organotypic cultures of nervous tissue. J
402 Neurosci Methods. 1991;37(2):173-82. PubMed PMID: 1715499.

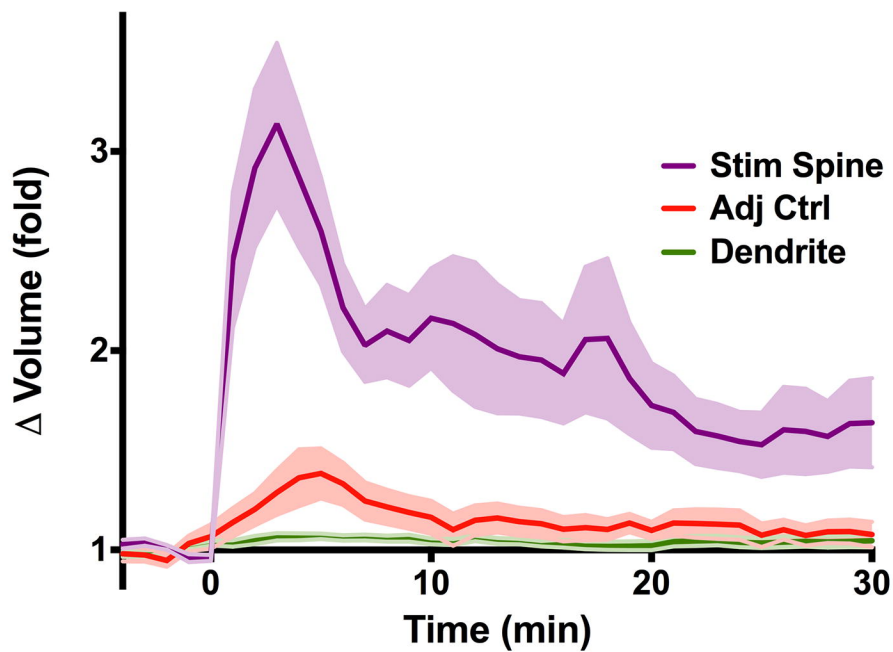
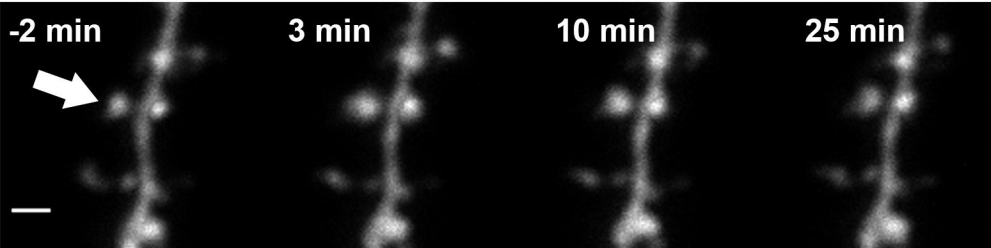




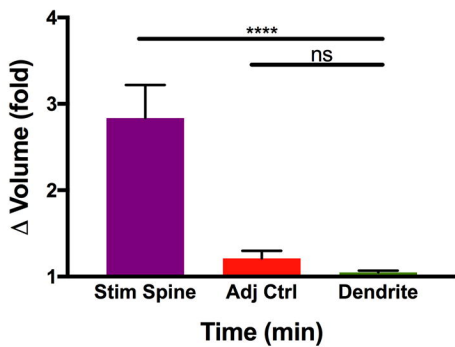
Autofocus Algorithm







Transient Phase



Sustained Phase

